A variable ULX and possible IMBH candidate in M51a

Hannah M. Earnshaw,[1]★ Timothy P. Roberts,[1] Lucy M. Heil,[2] Mar Mezcua,[3,4] Dominic J. Walton,[5] Chris Done,[1] Fiona A. Harrison,[5] George B. Lansbury,[1] Matthew J. Middleton[6] and Andrew D. Sutton[7]

[1]*Department of Physics, Centre for Extragalactic Astronomy, Durham University, South Road, Durham DH1 3LE, UK*

[2]*Anton Pannekoek Institute, Science Park 904, NL-1098 XH, Amsterdam, the Netherlands*

[3]*University of Montréal, Pavillon Roger-Gaudry (D-428), 2900 boul. Édouard-Montpetit, Montréal, QC H3T 1J4, Canada*

[4]*Harvard–Smithsonian Center for Astrophysics (CfA), 60 Garden Street, Cambridge, MA 02138, USA*

[5]*California Institute of Technology, Pasadena, CA 91125, USA*

[6]*Institute of Astronomy, University of Cambridge, Madingley Road, Cambridge CB3 0HA, UK*

[7]*Astrophysics Office, NASA Marshall Space Flight Center, ZP12, Huntsville, AL 35812, USA*

ABSTRACT

Ultraluminous X-ray source (ULX)-7, in the northern spiral arm of M51, demonstrates unusual behaviour for an ULX, with a hard X-ray spectrum but very high short-term variability. This suggests that it is not in a typical ultraluminous state. We analyse the source using archival data from *XMM–Newton*, *Chandra* and *NuSTAR*, and by examining optical and radio data from *HST* and Very Large Array. Our X-ray spectral analysis shows that the source has a hard power-law spectral shape with a photon index $\Gamma \sim 1.5$, which persists despite the source's X-ray luminosity varying by over an order of magnitude. The power spectrum of the source features a break at $6.5^{+0.5}_{-1.1} \times 10^{-3}$ Hz, from a low-frequency spectral index of $\alpha_1 = -0.1^{+0.5}_{-0.2}$ to a high-frequency spectral index of $\alpha_2 = 6.5^{+0.05}_{-0.14}$, making it analogous to the low-frequency break found in the power spectra of low/hard state black holes (BHs). We can take a lower frequency limit for a corresponding high-frequency break to calculate a BH mass upper limit of 1.6×10^3 M$_\odot$. Using the X-ray/radio Fundamental Plane, we calculate another upper limit to the BH mass of 3.5×10^4 M$_\odot$ for a BH in the low/hard state. The hard spectrum, high rms variability and mass limits are consistent with ULX-7 being an intermediate-mass BH; however we cannot exclude other interpretations of this source's interesting behaviour, most notably a neutron star with an extreme accretion rate.

Key words: accretion, accretion discs – stars: black holes – black hole physics – galaxies: individual: M51 – X-rays: binaries – X-rays: individual: M51 ULX-7.

1 INTRODUCTION

Ultraluminous X-ray sources (ULXs) are point sources that are located away from the centre of their host galaxies and have an X-ray luminosity $L_X > 10^{39}$ erg s^{-1}, the Eddington luminosity of a typical stellar-mass black hole (BH) with $M_{BH} \sim 10$ M$_\odot$ (Özel et al. 2010; see Feng & Soria 2011 for a review of ULXs). Many of these sources can be explained as stellar-mass BHs accreting at or close to the Eddington limit (e.g. Middleton et al. 2013). However for sources with $L_X > 3 \times 10^{39}$ erg s^{-1}, this is often not sufficient. Given that their non-nuclear nature rules out the sources being active galactic nuclei (AGNs), and assuming that they are not background sources erroneously associated with the galaxy, they require one of two alternative explanations. Either they are BHs of unusually high mass – that is, intermediate-mass BHs (IMBHs) with $10^2 \lesssim M_{BH} \lesssim 10^5$ M$_\odot$ (Colbert & Mushotzky 1999) – or they exhibit an extreme accretion mechanism beyond the standard thin disc scenario, such as super-Eddington accretion (Poutanen et al. 2007) and/or geometrically beamed emission (King et al. 2001).

The origin of IMBHs requires exotic formation scenarios, such as the collapse of early-Universe Population III stars (Madau & Rees 2001). This, and the results of studies implying that all but the brightest sources of the ULX population make up the high luminosity tail of the high mass X-ray binary (HMXB) luminosity function in spiral galaxies and the low mass X-ray binary luminosity function in elliptical galaxies (Swartz et al. 2004, 2011; Walton et al. 2011; Mineo, Gilfanov & Sunyaev 2012), points to the majority of ULXs being super-Eddington accreting stellar-mass sources. This is strengthened by results from the spectral analysis of these sources,

★ E-mail: hannah.earnshaw@durham.ac.uk

which exhibit a characteristic two-component spectrum with a soft excess and a high energy downturn at ~3–5 keV that is not found in sub-Eddington accretion states (e.g. Stobbart, Roberts & Wilms 2006; Gladstone, Roberts & Done 2009; Miyawaki et al. 2009). This downturn has been confirmed by observations of ULXs using *NuSTAR* (e.g. Bachetti et al. 2013; Walton et al. 2015).

There are currently a small number of good candidates for IMBHs. These tend to be objects too luminous to be explained by super-Eddington accretion on to stellar-mass BHs, in particular hyper-luminous sources (HLXs; $L_X > 10^{41}$ erg s^{-1}; Gao et al. 2003; Farrell et al. 2009; Sutton et al. 2012), or ULXs with powerful radio jets (e.g. Mezcua et al. 2013, 2015). For example one of the best HLX candidates, ESO 243-49 HLX-1 (henceforth HLX-1), has been observed in different spectral states similar to the hard and thermal dominated states seen in stellar-mass BH binaries (BHBs; Godet et al. 2009; Servillat et al. 2011). This strongly supports the interpretation of HLX-1 as a sub-Eddington accreting source scaled up to higher masses. If IMBHs do exist, then we might expect that some are accreting at lower rates and have a similar luminosity to stellar-mass ULXs, although distinguishing them from stellar-mass ULXs would be difficult and dependent on the spectral and timing properties of the source.

In order to study the properties of ULXs as a population, and to find the most likely candidates for IMBHs, we created a new, clean catalogue of candidate ULXs (Earnshaw et al., in preparation). This matched the 3*XMM*-DR4 data release of the *XMM–Newton* Serendipitous Sky Survey (Rosen et al. 2015) with the Third Reference Catalog of Bright Galaxies (de Vaucouleurs et al. 1991), using a method similar to Walton et al. (2011), with a number of improvements to reduce contamination by camera artefacts and background sources. This catalogue contains 331 candidate ULXs, which we searched for sources of interest on the basis of luminosity or variability. We found a small number of highly variable ULXs, including one particularly interesting source in M51.

The interacting galaxy system M51 (NGC 5194/5, also known as the Whirlpool Galaxy) is a pair of galaxies at a distance of 7.85 Mpc,[1] containing the face-on spiral galaxy M51a which has high rates of star formation and a large population of X-ray sources, including nine ULXs (Terashima, Inoue & Wilson 2006). One such ULX located in the northern spiral arm, henceforth referred to as ULX-7, has a hard X-ray spectrum and high levels of variability. Its variability was first investigated by Liu et al. (2002), who found a tentative period of 7620 s. Later studies (e.g. Terashima & Wilson 2004; Dewangan et al. 2005; Terashima et al. 2006) found significant long- and short-term variability, although they did not find a period, suggesting that the variability is instead due to aperiodic noise from stochastic processes. The source is near to a young massive star cluster with age $T \sim 12$ Myr (Abolmasov et al. 2007) and has previously been found to have a changing spectral shape by Yoshida et al. (2010), ranging from fairly flat ($\Gamma < 1.5$) to soft ($\Gamma \sim 2$–3), although any contribution from the host galaxy to the emission was not considered in their study.

While they often demonstrate spectral variability between observations (e.g. Kajava & Poutanen 2009), strong short-term variability is not a common feature of ULXs (e.g. Feng & Kaaret 2005; Heil, Vaughan & Roberts 2009). In the broadened disc/hard ultraluminous/soft ultraluminous classification of ULX accretion regimes, high (>10 per cent) fractional variability is predominantly seen in the soft ultraluminous state in which the X-ray spectrum is dominated by soft thermal emission (Sutton, Roberts & Middleton 2013). Furthermore, the variability is limited to the hard component of emission (Middleton et al. 2015a). A proposed mechanism for this is a clumpy wind that would be expected to be driven away from the disc by intense radiation pressure in super-Eddington accretion scenarios, and to intermittently obscure the hard central source in high-inclination systems, causing the spectrum to be dominated by soft thermal emission and variability to be imprinted on the hard emission component (e.g. Middleton et al. 2011, 2015a). However in the case of ULX-7, the spectrum is hard, which suggests that this source does not fit this model and may be in an accretion state more analogous to the low/hard state of stellar-mass BHs – in which case, this object might instead be a candidate IMBH, albeit emitting at a lower luminosity than other candidate IMBHs we are aware of to date.

Here we conduct our own analysis of ULX-7, examining its X-ray spectral and timing properties, as well as optical and radio data, to attempt to better characterize this fascinating source. In Section 2 we detail the reduction of archival data from *XMM–Newton*, *Chandra*, *NuSTAR*, the *Hubble Space Telescope* (*HST*) and the Very Large Array (VLA) telescopes. We present the results of our analysis in Section 3, and discuss the possibility of this source being a background AGN, a neutron star or an IMBH in Section 4, before presenting our conclusions in Section 5.

2 REDUCTION OF ARCHIVAL DATA

In this paper, we will investigate this object from a multiwavelength perspective, using archival data from a range of missions. We assume a source position of 13:30:01.0 +47:13:44 (J2000; Kilgard et al. 2005).

2.1 X-ray observations

There were six observations of M51 by the *XMM–Newton* observatory, using the European Photon Imaging Camera (EPIC), over the course of eight years, between 2003 and 2011. The durations of observations with *XMM–Newton* are limited by visibility due to the position of M51 in the sky and the orbit of the telescope. The longest observation to date is ~52 ks. Data reduction was performed using v13.5.0 of the *XMM–Newton* Scientific Analysis System (SAS) and up-to-date calibration files. We used EPPROC and EMPROC to produce calibrated event lists for the pn and MOS detectors. The event lists were filtered for high-energy background flaring in accordance with the standard *XMM–Newton* SAS threads,[2] excluding intervals for which the >10 keV count rate was ≥0.35 ct s^{-1} in the EPIC-MOS data and the 10–12 keV count rate was ≥0.4 ct s^{-1} in the EPIC-pn data.

XMM–Newton spectra and light curves were extracted using EVSELECT from 20 arcsec radius regions around the source, filtering for PATTERN≤12 for the EPIC-MOS camera and PATTERN≤4 for the EPIC-pn camera. Background counts were extracted from an equally sized region outside of the galaxy on the same chip, at a similar distance from the readout node. Redistribution matrices and auxilary response files were generated using RMFGEN and ARFGEN, respectively, and spectral data were grouped into bins of at least 25 counts, making sure not to oversample *XMM–Newton*'s intrinsic energy resolution by a factor more than 3. Corrected light curves

---

[1] The mean distance given by the NASA/IPAC Extragalactic Database (http://ned.ipac.caltech.edu/).

[2] See the SAS User Manual at http://xmm.esac.esa.int/sas.

Table 1. Dates, durations and fluxes for X-ray observations of M51 with *XMM–Newton*, *Chandra* and *NuSTAR*.

ID[a]	Observation ID	Instrument	Observation date	Exposure[b] (ks)	Flux[c] ($\times 10^{-13}$ erg cm^{-2} s^{-1})
			XMM–Newton		
X1	0112840201	MOS1	2003-01-15	20.66	1.9 ± 0.1
		MOS2		20.67	
		pn		19.05	
X2	0212480801	MOS1	2005-07-01	35.04	7.6 ± 0.2
		MOS2		35.77	
		pn		24.94	
X3	0303420101	MOS1	2006-05-20	39.60	5.9 ± 0.1
		MOS2		39.66	
		pn		30.90	
X4	0303420201	MOS1	2006-05-24	29.77	8.5 ± 0.2
		MOS2		29.76	
		pn		23.18	
X5	0677980701	MOS1	2011-06-07	9.80	5.2 ± 0.4
		MOS2		9.51	
		pn		5.13	
X6	0677980801	MOS1	2011-06-11	1.60	1.1 ± 0.1[d]
		MOS2		1.60	
		pn		2.30	
			Chandra		
C1	354	ACIS-S	2000-06-20	15.05	4.5 ± 0.5
C2	1622	ACIS-S	2001-06-23	27.15	0.5 ± 0.1[d]
C3	3932	ACIS-S	2003-08-08	48.61	4.7 ± 0.2
C4	12562	ACIS-S	2011-06-12	9.75	0.8 ± 0.1[d]
C5	12668	ACIS-S	2011-07-03	10.12	4.0 ± 0.6
C6	13812	ACIS-S	2012-09-12	159.54	7.1 ± 0.2
C7	13813	ACIS-S	2012-09-09	181.57	8.6 ± 0.2
C8	13814	ACIS-S	2012-09-22	192.36	5.5 ± 0.1
C9	13815	ACIS-S	2012-09-23	68.07	3.6 ± 0.2
C10	13816	ACIS-S	2012-09-26	74.07	0.8 ± 0.1
C11	15496	ACIS-S	2012-09-19	41.51	6.0 ± 0.3
C12	15553	ACIS-S	2012-10-10	38.07	0.3 ± 0.1[d]
			NuSTAR		
N1	60002038002	FPMA/B	2012-10-29	19	3.8 ± 0.7
					5.6 ± 0.9

[a]A short ID used elsewhere within this paper for clarity.

[b]Sum of the good time intervals after removal of background flaring events.

[c]Deabsorbed flux in the energy range 0.3–10 keV for *XMM–Newton* and *Chandra*, and the ranges 3–10 keV and 3–20 keV for *NuSTAR*. The flux is determined from the best-fitting power-law model, excluding contribution from soft diffuse emission in the *XMM–Newton* observations (see Section 3.1). The *NuSTAR* fluxes are calculated from the best-fitting power-law model (with $N_H = 1 \times 10^{21}$ cm^{-2}) to the 3–10 keV data and the 3–20 keV data, respectively.

[d]Where there is insufficient data to calculate flux from a best-fitting model, we use WebPIMMS to find the deabsorbed flux, using the detected count rate and a power-law model with $N_H = 1 \times 10^{21}$ cm^{-2} and $\Gamma = 1.5$.

for EPIC-MOS and EPIC-pn were generated using EPICLCCORR with a bin size of 50 s and added together, using the same start and end times. All six observations have a quality warning flag due to the source being located within bright extended emission, which we characterize in Section 2.1.

While *Chandra* does not have the collecting area of *XMM–Newton*, it is not limited by visibility in the same way, and its orbit allows for far longer observations of M51. There have been 11 *Chandra* observations of M51 taken over the course of 12 yr, between 2000 and 2012, the longest being ∼190 ks (see Table 1) during a set of five deep observations in 2012. The *Chandra* data were reduced using v4.7 of the *Chandra* Interactive Analysis of Observations (CIAO) software package and reprocessed to produce up-to-date event lists.

Chandra spectra and light curves were extracted using the SPECEXTRACT and DMEXTRACT routines, respectively, from 3 arcsec radius re-

gions, with the same binning as the *XMM–Newton* data. Since ULX-7 is a point source, we set weight=no and correctpsf=yes. Background counts were collected from an annulus around the source between 3 and 20 arcsec. This same annulus was also used to characterize diffuse emission surrounding the object in order to correct the *XMM–Newton* spectra – the background region in this case was taken from an equally sized region outside of the galaxy. Between *XMM–Newton* and *Chandra*, we can examine the long-term variability of the source, as well as its short-term properties.

The advent of the *NuSTAR* mission allows us to probe spectral energies of >10 keV for resolved sources. To date there is one observation of M51 using *NuSTAR*, performed in 2012, in which ULX-7 is detected along with the low-luminosity AGN and one other ULX in the galaxy. We reduced the *NuSTAR* data using the standard pipeline, NUPIPELINE, part of the *NuSTAR* Data Analysis Software (NUSTARDAS, v1.4.1; included in the HEASOFT distribution), with the

instrumental calibration files from CALDB v20140414. The unfiltered event files were cleaned with the standard depth correction, significantly reducing the internal high-energy background, and passages through the South Atlantic Anomaly were removed. Source spectra and instrumental responses were produced for each of the two focal plane modules (FPMA/B) using NUPRODUCTS. Source spectra were extracted from a circular region of radius 25 arcsec in order to avoid contamination from a potential nearby X-ray source, while background was estimated from a much larger region on the same detector as the source, avoiding all the other bright X-ray sources in M51. In order to maximize the good exposure, in addition to the standard (mode 1) data, we also reduce the available mode 6 data; see Walton et al. (in preparation) and Fuerst et al. (in preparation) for a description of *NuSTAR* mode 6. This provides an additional ∼15 per cent exposure, resulting in a total on-source time of 19 ks per FPM. Finally, owing to the low signal to noise, we combined the data from FPMA and FPMB using ADDASCASPEC. The resulting *NuSTAR* spectrum provides a detection up to ∼20–25 keV, and is rebinned to a minimum of 20 counts per bin for our spectral analysis.

A list of all X-ray observations is presented in Table 1. We calculate the flux between 0.3 and 10 keV (3.0–10 keV and 3.0–20 keV for the *NuSTAR* data) using the best-fitting absorbed power-law model if there are sufficient counts for a spectral fit. In the cases where there are a small number of data points we use WebPIMMS[3] and the count rate to predict the flux, assuming a photon index of $\Gamma = 1.5$ (the average photon index of the best-fitting models to the data we were able to fit – see Section 3.1). In the case of *XMM–Newton* observation X6, it should be noted that the flux is likely dominated by the surrounding diffuse emission rather than the source itself. The source flux varies between 3.0×10^{-14} erg cm^{-2} s^{-1} and 8.6×10^{-13} erg cm^{-2} s^{-1} in the 0.3–10 keV energy band over the course of all observations (i.e. its luminosity varies between 2.2×10^{38} erg s^{-1} and 5.1×10^{39} erg s^{-1}). This is an unusually high amount of flux variation for a ULX, even if we disregard fluxes calculated using WebPIMMS, in which case we still see variation of over an order of magnitude.

2.2 Radio observations

In order to search for core radio emission from the ULX, we retrieved archival VLA A-array data at 1.5 GHz (project 11A142, 2011 August). The data flagging and calibration was performed following standard procedures with the Common Astronomy Software Applications (CASA) software. The data were calibrated in amplitude using 3C286 as flux calibrator, while delay and phase solutions were derived from the phase calibrator J1327+4326 and interpolated and applied to the target source. The calibrated data were imaged in CASA using the Cotton–Schwab algorithm and natural weighting. The resulting beam has a size of 1.5 arcsec × 1.4 arcsec oriented at a position angle of 36°.9. No radio emission is detected at the *Chandra* position of the source within a positional error of 1 arcsec. An upper limit on the 1.5 GHz radio flux density of 87 μJy beam^{-1} is derived from the local rms at the *Chandra* position. The 1.5 GHz radio image is shown in Fig. 1. Other studies of the radio emission in M51 have also not detected a counterpart to ULX-7 (Maddox et al. 2007; Rampadarath et al. 2015).
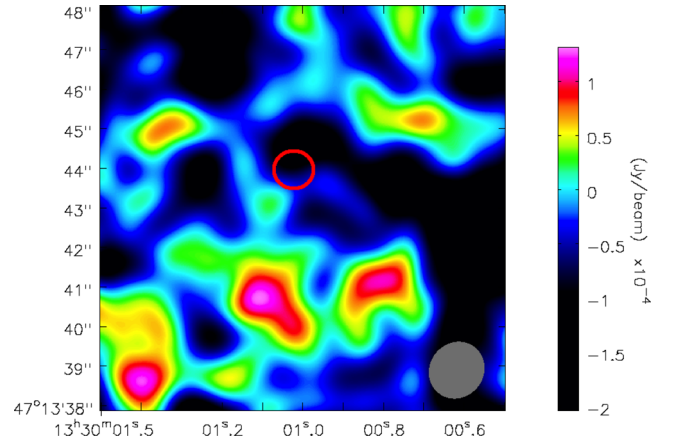
Figure 1. The 1.5 GHz radio image surrounding the source location, which is marked with a 1 arcsec error circle (red) and does not coincide with a radio detection. The rms is 8.73×10^{-5} Jy beam^{-1}, therefore the fluctuations shown are all consistent with noise. The beam size is marked in grey.

2.3 Optical observations

M51 has been well observed by *HST* over the course of the mission's lifetime, and was mapped in 2005 with the Advanced Camera for Surveys/Wide Field Channel camera as part of the Hubble Heritage project. We collected pre-processed data from the Hubble Legacy Archive, made up of exposures combined using the MULTIDRIZZLE routine. We used images in the *F435W* (*B*), *F555W* (*V*) and *F814W* (*I*) bands to locate possible optical counterparts to ULX-7. The 90 per cent confidence circle for the *Chandra* ACIS-S instrument is 0.6 arcsec, however it is also necessary to align the relative astrometry of the *HST* and *Chandra* images. We did this by selecting *2MASS* objects within the M51 field and using the IRAF tools CCFIND, CCMAP and CCSETWCS to find the necessary corrections to the right ascension and declination. We found an offset of 0.1 arcsec in the right ascension direction and 0.7 arcsec in declination.

The source is located near to a young star cluster and has a number of possible optical counterparts. We performed photometry on these objects using the DAOPHOT II/ALLSTAR software package (Stetson 1987), a PSF-fitting routine (see Section 3.3), although due to the crowded nature of the field, we were only able to obtain limited constraints on the magnitudes in each band. Where the magnitude of an object was unconstrained, we used the various sources of detector noise to place a lower limit on the magnitude.

3 ANALYSIS AND RESULTS

We analysed the archival data described in Section 2 in order to determine the properties of ULX-7. Optical and X-ray images of M51 from the *HST*, *XMM–Newton*, *Chandra* and *NuSTAR* telescopes, along with the location of ULX-7, are shown in Fig. 2. The source lies within diffuse X-ray emission in the northern spiral arm of its host galaxy.

3.1 X-ray imaging and spectral analysis

The *XMM–Newton* image of the source and its environment (see Fig. 2) shows that it lies within extended diffuse emission. Therefore, the *XMM–Newton* source spectra are likely to be contaminated by a soft thermal component. In order to characterize this component, we first examine archival data from the *Chandra* observatory,
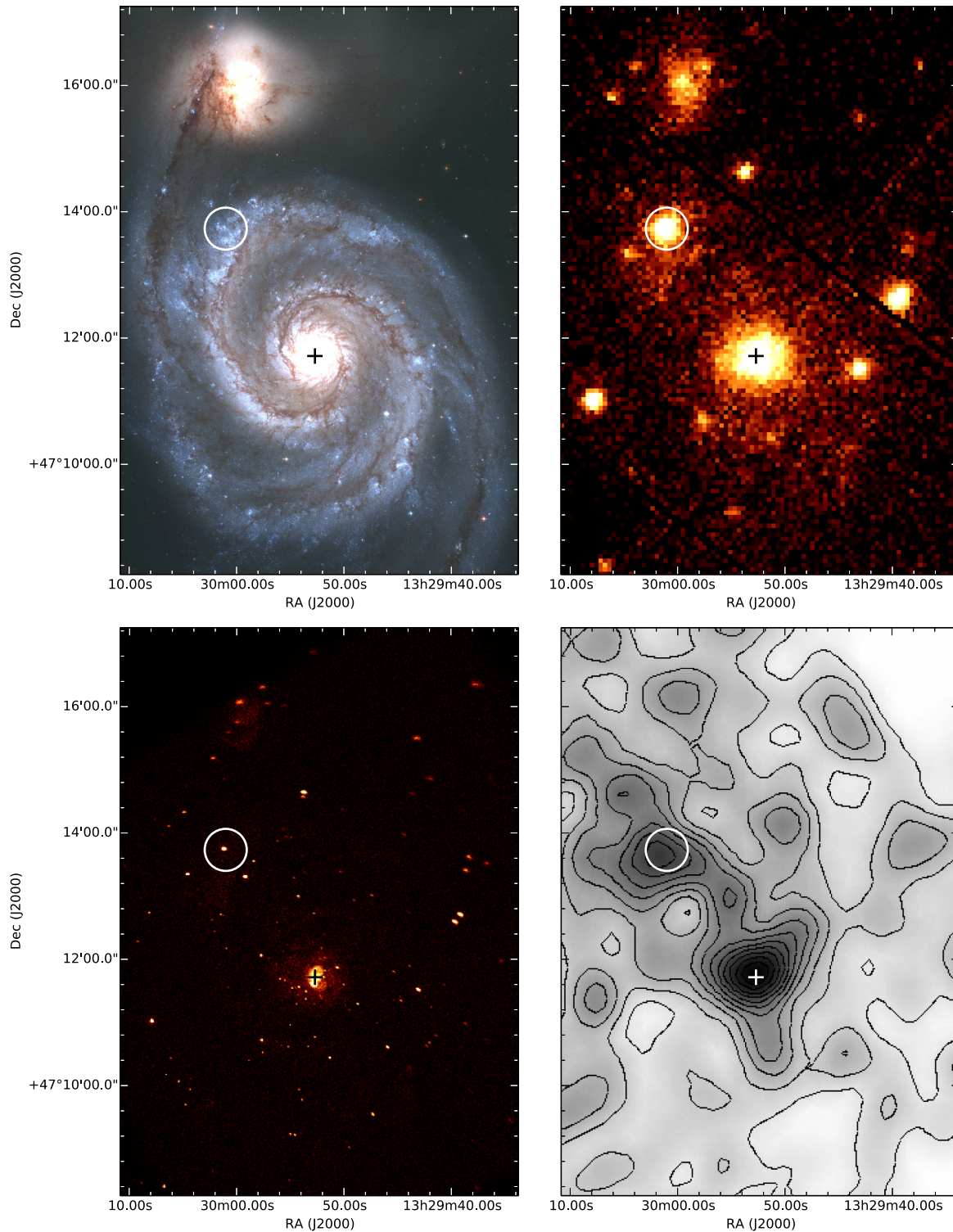
Figure 2. Images of the M51 system, centred for convenience on 13:29:52.3 +47:12:45.3 (J2000). In all images, the position of the centre of M51a is marked with a cross, and ULX-7 is indicated by a 20 arcsec radius white circle. Top left, *HST* true-colour image with the red, green and blue channels corresponding to the *F*814*W*, *F*555*W* and *F*435*W* bands, respectively. Top right, *XMM–Newton* EPIC-pn image in the energy range 0.3–10 keV from observation X4. Bottom left, *Chandra* ACIS-S image in the energy range 0.3–10 keV from observation C8. Bottom right, *NuSTAR* image in the energy range 3–24 keV, smoothed with a 14 arcsec Gaussian and with contours to aid visibility only.

since its high spatial resolving power allows us to separate out the spectra of the source and of the surrounding gas.

To obtain sufficient counts from the *Chandra* data for analysis, we used only the five observations with exposure time >50 ks.

We extracted diffuse emission spectra from an annulus with an inner radius of 3 arcsec around the source, and an outer radius of 20 arcsec to be the same as the *XMM–Newton* footprint used for source analysis. There are no resolved point sources within the

Table 2. The temperature, flux and χ^2 goodness of fit for the two MEKAL components used to fit the diffuse emission around ULX-7 in the deepest *Chandra* observations.

ID[a]	kT_1 (keV)	F_1 ($\times 10^{-14}$ erg cm^{-2} s^{-1})	kT_2 (keV)	F_2 ($\times 10^{-14}$ erg cm^{-2} s^{-1})	χ^2/dof
C6	$0.25^{+0.08}_{-0.07}$	1.3 ± 0.3	$0.6^{+0.4}_{-0.1}$	1.3 ± 0.3	54.3/60
C7	$0.22^{+0.05}_{-0.04}$	1.5 ± 0.4	$0.7^{+0.2}_{-0.1}$	1.0 ± 0.2	84.2/73
C8	$0.17^{+0.10}_{-0.09}$	1.0 ± 0.3	$0.4^{+0.2}_{-0.1}$	1.4 ± 0.2	76.2/71
C9	<0.27	2.5 ± 0.4	<1.0	0.5 ± 0.2	14.1/21
C10	$0.24^{+0.05}_{-0.06}$	2.0 ± 0.4	$0.8^{+0.6}_{-0.2}$	0.5 ± 0.3	34.4/24
All[b]	$0.26^{+0.03}_{-0.05}$	1.9 ± 0.1	0.8 ± 0.2	0.6 ± 0.1	279.9/258

Notes. [a]The short observation ID as defined in Table 1. [b]The best-fitting parameters when fitting all five observations simultaneously.

annulus. We took a background spectrum from a 20 arcsec radius region centred to the north of the galaxy in an area with minimal diffuse emission.

All spectral fitting was performed with v12 of XSPEC (Arnaud 1996), and all *Chandra* and *XMM–Newton* observations are fitted in the 0.3–10 keV energy range with errors given at 90 per cent confidence intervals. The data is binned (see Section 2.1) such that fitting can be performed using χ^2 minimization, and χ^2 statistics used to determine the goodness-of-fit. The abundance tables of Wilms, Allen & McCray (2000) are used throughout.

The diffuse emission spectra were well-fitted using two MEKAL thermal plasma components: a cooler component at ~0.2 keV and a second warmer component at ~0.7 keV, consistent with previous studies into the diffuse emission of the galaxy (e.g. Owen & Warwick 2009). We also detected hard emission, requiring an additional hard component in the spectrum since attempting to fit the data without it causes one of the MEKAL components to take on an unrealistically high temperature. This hard component may be due to unresolved hard sources within the annulus, therefore we fitted it with an absorbed power law (`tbabs*powerlaw`), allowing the photon index to vary. We set the hydrogen column density to $N_{\rm H} = 1 \times 10^{21}$ cm^{-2} since preliminary fits to the ULX-7 source spectrum gave $N_{\rm H}$ of approximately this value and we would expect absorption by the surrounding interstellar medium (ISM) to be similar in the near vicinity. The power law has Γ ~1–2 and would contribute <0.1 per cent of the total flux when combined with the source spectrum. For this reason, we expect that its effect on the spectrum of ULX-7 is negligible, so we do not include it in our characterization of the diffuse emission itself.

The fit results for the diffuse emission are given in Table 2. Given that the temperature parameters are all consistent within the errors, and that we do not expect the diffuse emission to vary between observations if it originates in the ISM of M51, we performed a simultaneous fit of all five observations and used the best-fitting parameters (see Table 2) when fitting the *XMM–Newton* source spectra. An example of the diffuse emission spectrum is shown in Fig. 3.

While six *XMM–Newton* observations of ULX-7 exist, there is only sufficient data quality for spectral analysis from the first five. We fit the spectra of each of these first five observations with an absorbed power-law model and two additional MEKAL components to account for contamination from the diffuse emission (`mekal+mekal+tbabs*powerlaw`). We set the lower
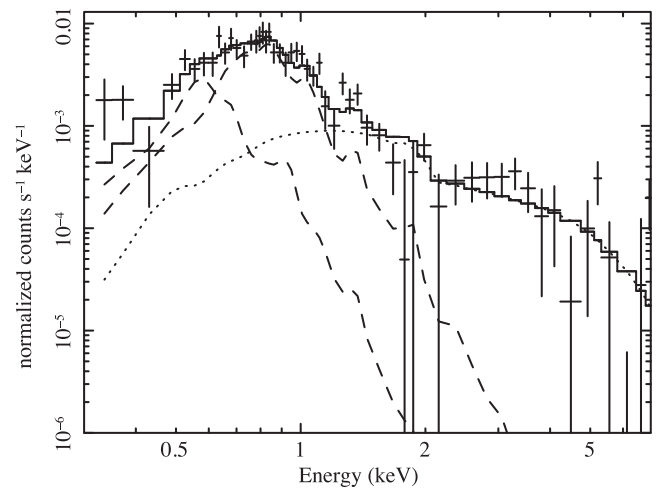

Figure 3. The X-ray spectrum of the diffuse emission surrounding ULX-7 from observation C8, together with the best-fitting `mekal+mekal+tbabs*powerlaw` model, with MEKAL parameters as given in Table 2. The MEKAL components are plotted with dashed lines and the `tbabs*powerlaw` component with a dotted line. Events are grouped into 20 counts per bin.

bound of $N_{\rm H}$ for the `tbabs` component to the Galactic foreground value[4] of $N_{\rm H} = 1.8 \times 10^{20}$ cm^{-2} and fixed the MEKAL parameters and normalizations to the average values determined from the *Chandra* results, which we take as a good first-order approximation to the contribution of diffuse emission to the spectrum. Most of the *XMM–Newton* source spectra are well-fitted by this model and exhibit fairly hard ($\Gamma \sim 1.5$–1.6) power-law emission. The exception is observation X3 for which we reject a simple absorbed power law at $>4\sigma$ significance. The fit for X3 undergoes moderate improvement ($\Delta\chi^2 \sim 17$ for 2 fewer degrees of freedom) by the addition of a multicolour disc component (`mekal+mekal+tbabs*(diskBB+powerlaw)`), although it is still rejected at ~3.5σ significance. It is unclear from the residuals what a better model might be, so we are unable to find an acceptable fit for the data from this observation. It is possible that ULX-7 exhibits similar soft atomic features to those seen in other ULXs

[4] Foreground $N_{\rm H}$ was obtained from the HEASARC $N_{\rm H}$ calculator at http://heasarc.gsfc.nasa.gov/cgi-bin/Tools/w3nh/w3nh.pl, using results from Kalberla et al. (2005).

Table 3. The parameter values and goodness of fit for the *XMM–Newton* and *Chandra* source spectra when fitted with an absorbed power-law model (and a power law with a multicolour accretion disc in the case of X3).

ID[a]	N_H ($\times 10^{21}$ cm^{-2})	Γ	T_{in} (keV)	χ^2/dof
		XMM–Newton		
X1	$0.6^{+0.6}_{-0.5}$	1.7 ± 0.2	–	47.9/53
X2	1.1 ± 0.2	1.59 ± 0.06	–	231.2/177
X3	1.1 ± 0.2	$1.57^{+0.07}_{-0.06}$	–	260.5/174
	1.2 ± 0.4	1.2 ± 0.2	0.4 ± 0.1	243.7/172
X4	0.8 ± 0.2	$1.45^{+0.06}_{-0.05}$	–	172.3/182
X5	$0.6^{+0.6}_{-0.5}$	$1.5^{+0.2}_{-0.1}$	–	30.5/39
		Chandra		
C1	$1.5^{+0.9}_{-0.8}$	1.3 ± 0.2	–	26.2/28
C3	1.4 ± 0.4	1.5 ± 0.1	–	67.2/94
C5	$0.4^{+4.0}_{-0.4}$	$1.3^{+0.5}_{-0.3}$	–	13.7/12
C6	1.2 ± 0.2	1.49 ± 0.05	–	244.1/215
C7	1.4 ± 0.2	$1.48^{+0.05}_{-0.04}$	–	273.1/245
C8	$1.6^{+0.3}_{-0.2}$	$1.54^{+0.06}_{-0.05}$	–	203.6/203
C9	$1.2^{+0.6}_{-0.5}$	1.4 ± 0.1	–	65.9/69
C10	1.0^b	1.5 ± 0.2	–	32.4/20
C11	1.0 ± 0.5	1.5 ± 0.1	–	89.3/94

[a]The short observation ID as defined in Table 1.
[b]N_H frozen at 1×10^{21} cm^{-2}.

(e.g. Middleton et al. 2015b), however the presence of diffuse emission in the host galaxy complicates more detailed study of the soft end of the spectrum.

We also fit the *Chandra* source observations of sufficient data quality with an absorbed power-law model to ensure that they are consistent with the *XMM–Newton* results (we do not include the MEKAL components as we assume that the contribution from surrounding diffuse emission is negligible in the *Chandra* source data). As in the case of *XMM–Newton*, N_H is given a lower limit of the Galactic foreground value and allowed us to vary, except for observation C10 for which we set N_H to 1×10^{21} cm^{-2} (the average value found from fits to other observations) since there is insufficient data to constrain it further. We find that the spectra are consistent with the same hard ($\Gamma \sim 1.5$) power-law shape as the *XMM–Newton* observations.

Best-fitting parameter values for *XMM–Newton* and *Chandra* are given in Table 3, and examples of high- and low-flux spectra and their power-law fits are shown in Fig. 4.

ULX-7 is strongly detected in the 8–24 keV band in the *NuSTAR* observation (Fig. 2), with a good signal found up to ~ 20 keV (Fig. 5). The data quality is insufficient to perform in-depth analysis, however we are still able to extract a spectrum from a circular region with radius of 25 arcsec. The *NuSTAR* spectrum is plotted alongside the *XMM–Newton* observation X2 and the *Chandra* observation C6 in Fig. 6. These are the observations closest in flux to the *NuSTAR* observation with the 3–10 keV flux of the best-fitting absorbed power-law model being $(3.80 \pm 0.09) \times 10^{-13}$ and $(3.9 \pm 0.2) \times 10^{-13}$ erg cm^{-2} s^{-1} for X2 and C6, respectively. The *NuSTAR* 3–10 keV data has a flux of $(3.8 \pm 0.7) \times 10^{-13}$ erg cm^{-2} s^{-1} when fitted with an absorbed power-law model, having $\Gamma = 1.3 \pm 0.7$ (with N_H fixed at 1×10^{21} cm^{-2}, the average value found from *XMM–Newton* and

Chandra observations, since the *NuSTAR* data is too high energy to constrain it).

The full 3–20 keV *NuSTAR* data demonstrates a softer spectrum when fitted with a power-law model, with $\Gamma = 2.1 \pm 0.3$. This suggests that the spectrum turns over at the higher energies we observe with *NuSTAR*. Therefore, we fit the *NuSTAR* data simultaneously with observations X2 and C6, with an absorbed power-law model (and a background modelled with MEKAL components for the *XMM–Newton* observation as before). We also fit a model replacing the `powerlaw` component with a `cutoffpl` component to characterize any potential turnover. In both cases we also included a multiplicative constant to the absorbed power-law component of the models, which we allowed to vary freely to account for any difference in normalization between *NuSTAR* and the other telescope. The fit parameters with *NuSTAR* data included are given in Table 4, although it is important to note that neither of these observations are contemporaneous with the *NuSTAR* observation and so we cannot be certain that the source is in the same spectral state between them.

While both observations are consistent with a cut-off to the energy spectrum at 18 keV, we find that a cut-off power-law model offers no improvement over a power-law model for either observation X2 or C6. This is not entirely unexpected, as the appearance of a turnover is mainly driven by a single *NuSTAR* data point. Further observations with *NuSTAR* simultaneous with observations from *XMM–Newton* are required to better constrain the high-energy spectral shape of this source.

3.2 Timing analysis

All observations of ULX-7 with *XMM–Newton* are flagged as variable in the *XMM–Newton* Serendipitous Source Catalogue, and all have fractional rms at ~ 30–40 per cent according to an initial examination of the light curves using the LCSTATS routine in FTOOLS. Previous studies have attempted to find a period in this variability, with Liu et al. (2002) suggesting a period of 7620 s using EFSEARCH and Dewangan et al. (2005) similarly declaring a period of 5925 s with $\sim 2\sigma$ significance. However, a subsequent study by Terashima et al. (2006) found no evidence of periodic variation, instead suggesting that the source variability is due to stochastic noise.

The source also undergoes significant long-term variation, with the dynamic range of its flux encompassing well over an order of magnitude, even over the course of a single month when observed using *Chandra* in 2012. The long-term light curve, along with an example of short-term variability from observation X3, is shown in Fig. 7. However, despite this variation in flux there is no evidence for a flux–hardness relation, given the consistent shape of the spectrum found in Section 3.1.

We created power spectra for the *XMM–Newton* and *Chandra* observations of ULX-7 by taking the periodogram of fixed-length segments in each observation taken from good time intervals and averaging over all segments for each telescope. We used 3200 s segments for the *XMM–Newton* observations and 12 800 s segments for the *Chandra* observations. The greater length of the *Chandra* observations allows us to probe down to $\sim 10^{-4}$ Hz, although at higher frequencies the data is dominated by noise, whereas the *XMM–Newton* data, while not having the low-frequency range, has far less contribution from white noise up to $\sim 8 \times 10^{-3}$ Hz. The two data sets are therefore very complementary and allow us access to two decades of frequency space.

The power spectra are normalized so that the power is given in units of the squared fractional rms per frequency interval. We combined all observations for each telescope, given that the overall
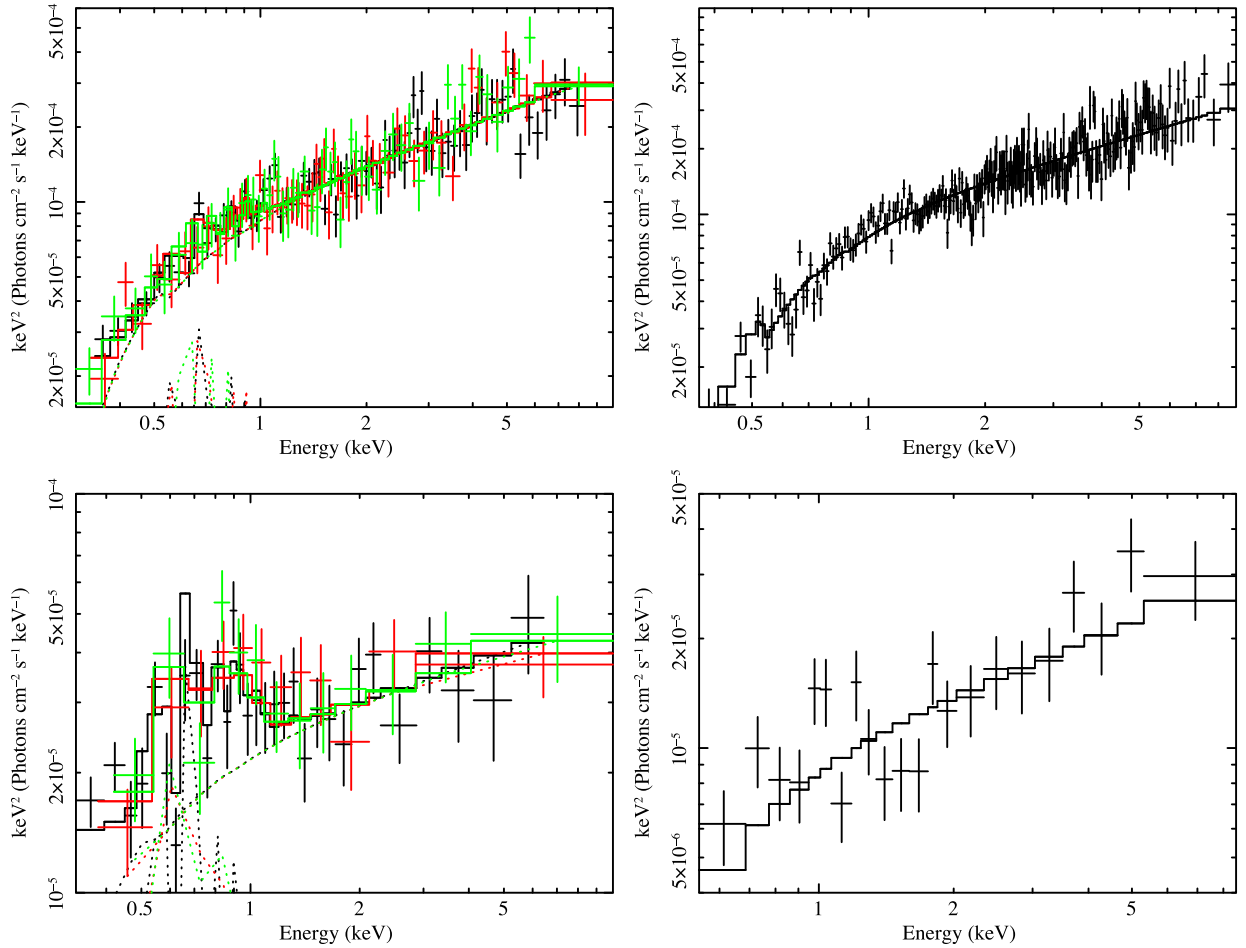
Figure 4. Example spectra of ULX-7 from *XMM–Newton* and *Chandra* at high and low fluxes, unfolded from the detector response and plotted between 0.3 and 10 keV, along with the best-fitting absorbed power-law model and the contribution from diffuse emission in the case of *XMM–Newton*. Fluxes can be found in Table 1, the diffuse emission parameters in Table 2, and best-fitting source parameters in Table 3. For the *XMM–Newton* spectra, pn data is plotted in black, MOS1 data in red and MOS2 in green. Top left, high-flux *XMM–Newton* observation X4. Top right, high-flux *Chandra* observation C7. Bottom left, low-flux *XMM–Newton* observation X1. Diffuse emission can be seen to be dominant at the soft end of this spectrum (<1 keV). Bottom right, low-flux *Chandra* observation C10.

shape of the power spectrum remained consistent from observation to observation, except for *Chandra* observations C4 and C5, which did not have good time intervals long enough for our chosen segment length, and C12, which contributed a lot of noise to the power spectrum due to a very low count rate.

We first rule out a simple power-law shape to the power spectrum by performing a simultaneous fit to the *XMM–Newton* and *Chandra* data using the whittle statistic in XSPEC and a powerlaw model, disregarding frequency bins consistent with the white noise level of the power spectrum. The best-fitting power law has $\alpha = 0.4$ (for $P(\nu) \propto \nu^{-\alpha}$) which has $\chi^2 = 54.8/28$ and we reject at $>3\sigma$ significance, so we can be confident that the power spectrum shape requires a more complex model to fit it. We next fit the power spectrum with a broken power-law model. This is an excellent fit to the data, with goodness-of-fit $\chi^2 = 23.0/25$, however the fit parameters are not highly constrained. We find that the power spectrum exhibits a break at $\nu_b = 6.5^{+0.5}_{-1.1} \times 10^{-4}$ Hz, with a low-frequency slope of $\alpha_1 = -0.1^{+0.5}_{-0.2}$ and a high-frequency slope of $\alpha_2 = 0.65^{+0.05}_{-0.14}$ (errors were found using a Monte Carlo Markov Chain method with a chain length of 100 000). Since the break is at the overlap of the two power spectra and its frequency can only be constrained with the *Chandra* data, it is likely that future long observations with *XMM–Newton*
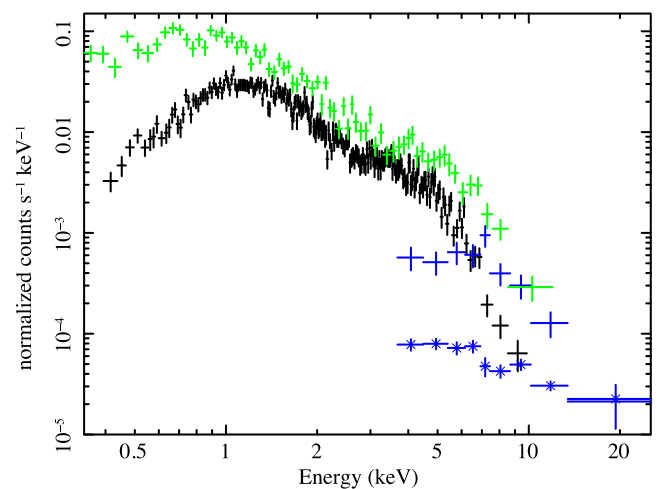

Figure 5. The data spectra of the source from *XMM–Newton* observation X2 (green – only EPIC-pn data is shown for clarity), *Chandra* observation C6 (black) and combined FPMA and FPMB data from *NuSTAR* (blue), along with the *NuSTAR* background spectrum (blue crosses). We detect a good signal from *NuSTAR* up to ∼20 keV.
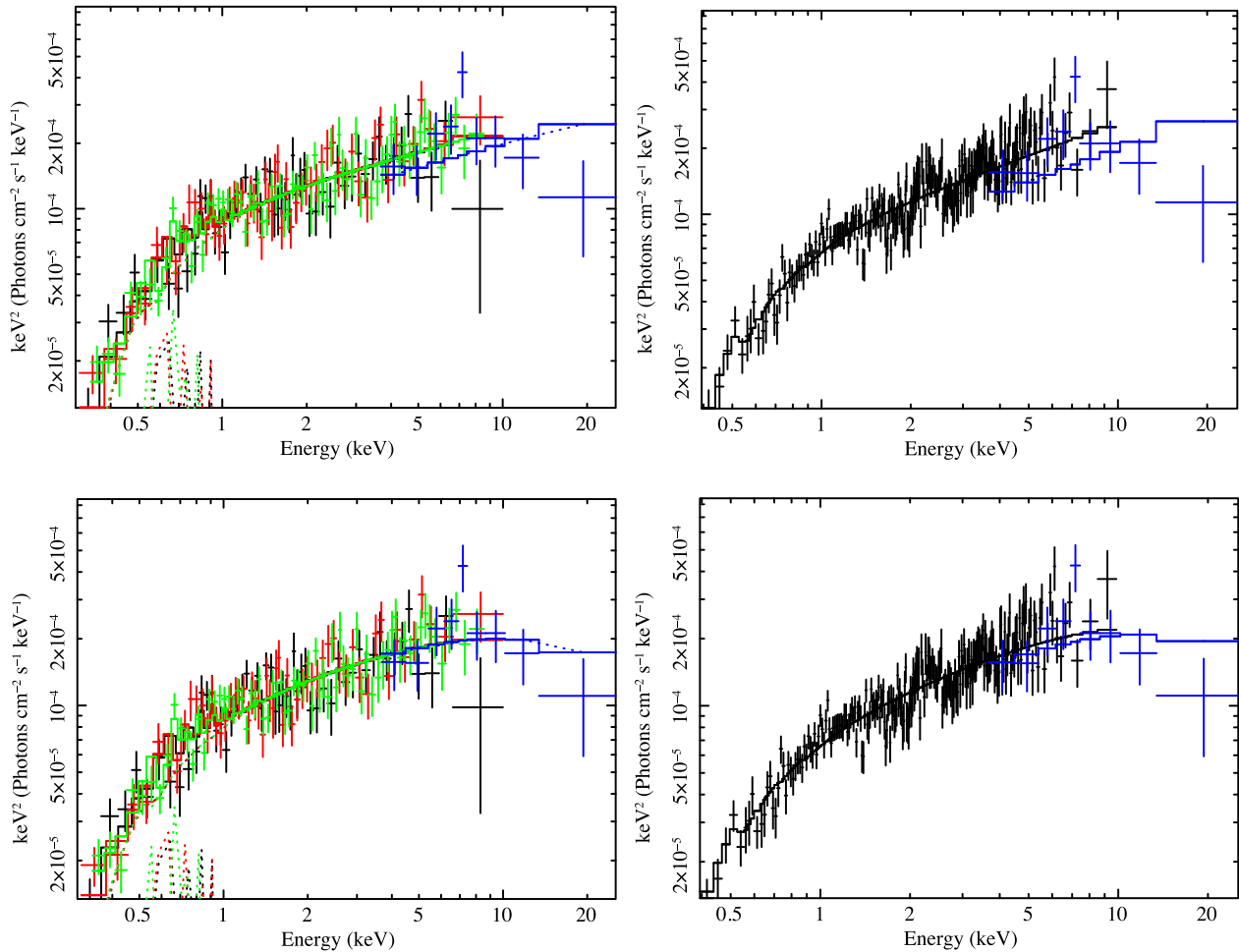
Figure 6. Spectra of ULX-7 from *XMM–Newton* observation X2 and *Chandra* observation C6, unfolded from the detector response and plotted between 0.3 and 10 keV, with the combined FPMA and FPMB data from *NuSTAR* plotted between 3 and ∼20 keV (blue). *XMM–Newton* spectra colours are as Fig. 4. Top left, X2 and *NuSTAR* data, fitted with a `mekal+mekal+tbabs*powerlaw` model. Top right, C6 and *NuSTAR* data, fitted with a `tbabs*powerlaw` model. Bottom left, X2 and *NuSTAR* data, fitted with a `mekal+mekal+tbabs*cutoffpl` model. Bottom right, C6 and *NuSTAR* data, fitted with a `tbabs*cutoffpl` model.

will help to better characterize the break. The power spectra for the two telescopes are shown in Fig. 8.

In order to see how the fractional variability of ULX-7 changes as a function of energy, we created a fractional rms spectrum using five energy bands by integrating over the power spectrum for each energy band, averaging over all *XMM–Newton* segments. Since the source flux is contaminated by diffuse emission that we do not expect to be variable, we also correct for the flux contribution from the diffuse emission, giving the intrinsic fractional variability of the source. The source exhibits a high amount of variability across all energy bands, especially at low and high energies, although we find the spectrum to be consistent with constant fractional rms at all energies. The fractional rms spectrum is shown in Fig. 9.

We also checked for an rms–flux relation by ordering intervals by flux and grouping them into bins of at least 10 before creating an unnormalised power spectrum for each bin and integrating over a decade in frequency to find the rms. The data was sufficient to confirm that ULX-7 exhibits a positive linear rms–flux relation as expected for an accreting source (Heil, Vaughan & Uttley 2012), with a significance of >10σ for a positive slope. The rms–flux relations are shown in Fig. 10. ULX-7 is the third ULX to date

Table 4. Parameter values and goodness of fit for the *NuSTAR* spectrum fit simultaneously with the closest-flux observations X2 and C6, with both a power-law (top) and a cut-off power-law (bottom) model.

ID	N_H ($\times 10^{21}$ cm^{-2})	Γ	E_{cut} (keV)	χ^2/dof
X2	1.4 ± 0.3	1.64 ± 0.06	–	245.0/184
	1.1 ± 0.3	1.5 ± 0.1	18^{+51}_{-8}	239.9/183
C6	1.3 ± 0.2	1.51 ± 0.05	–	264.5/223
	1.1 ± 0.3	1.3 ± 0.1	18^{+43}_{-8}	258.8/222

for which a positive linear rms–flux relation has been confirmed (Hernández-García et al. 2015).

Finally, we also examine the data from the *XMM–Newton* EPIC-pn camera, which has a time resolution of 73.4 ms in full-frame mode, for evidence of coherent pulsations such as those produced by pulsars. To do this we use the *H*-test (de Jager, Raubenheimer & Swanepoel 1989). In brief, the *H*-test is a test for a periodic signal that is especially useful in the case where there is no a priori information about the shape of the light curve available. The *H*
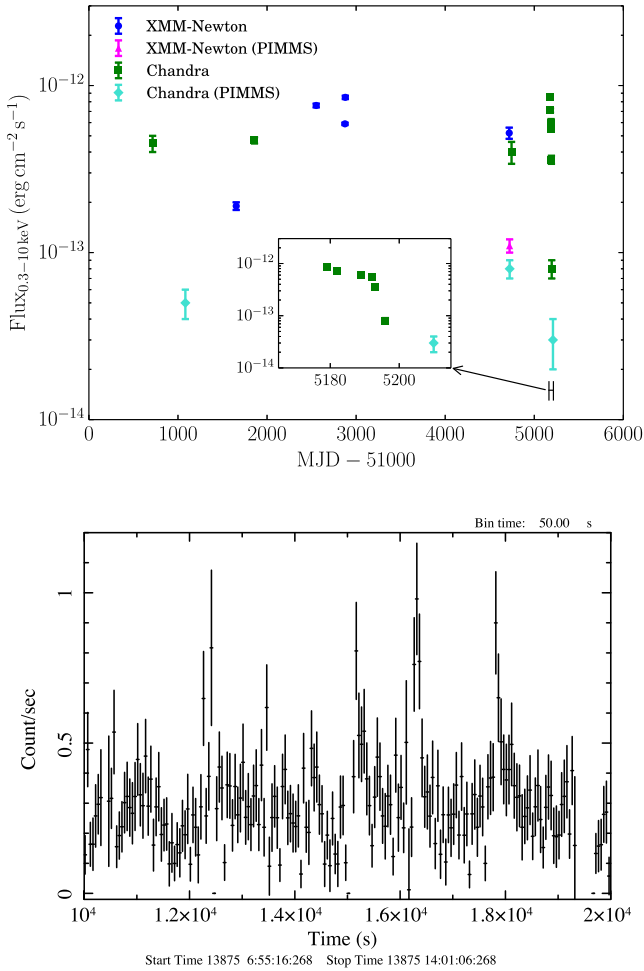
Figure 7. Top, the long-term light curve for ULX-7 showing the 0.3–10 keV flux over time as measured using the *XMM–Newton* and *Chandra* telescopes. Points identified as PIMMS are fluxes calculated from the count rate assuming a power-law spectrum with $N_{\rm H} = 1 \times 10^{21}$ cm^{-2} and $\Gamma = 1.5$. See Table 1 for details and values. Bottom, a 10 ks segment of the pn + MOS light curve of observation X3, binned into 50 s intervals.

statistic is based on the Z_m^2 statistic (Buccheri et al. 1983), and defines the optimal number of harmonics, M, such that:

$$H \equiv \max_{1 \le m \le 20} \left(Z_m^2 + 4m + 4 \right) = Z_M^2 + 4M + 4 \ge 0. \tag{1}$$

We apply the H-test to the five longest *XMM–Newton* observations, examining a range of frequencies from 6.85 Hz (approximately the Nyquist frequency for EPIC-pn data) to 0.1 Hz. We found no evidence of a pulsation period to high significance (that is, the commonly quoted condition of $H > 23$), although we found three marginally significant periods with $H > 17$, equivalent to a probability of $p \lesssim 10^{-3}$ that these H values were produced by chance, which are listed in Table 5. It should be noted that a period of 0.3003 s is approximately four times the time resolution of the EPIC-pn camera.

3.3 Optical counterparts

We mark the *Chandra* position of ULX-7 on a true-colour *HST* image with a 0.6 arcsec radius 90 per cent confidence circle in Fig. 11. Using DAOPHOT II, we were able to obtain photometric data for 11 objects within the circle, although visual inspection reveals that there
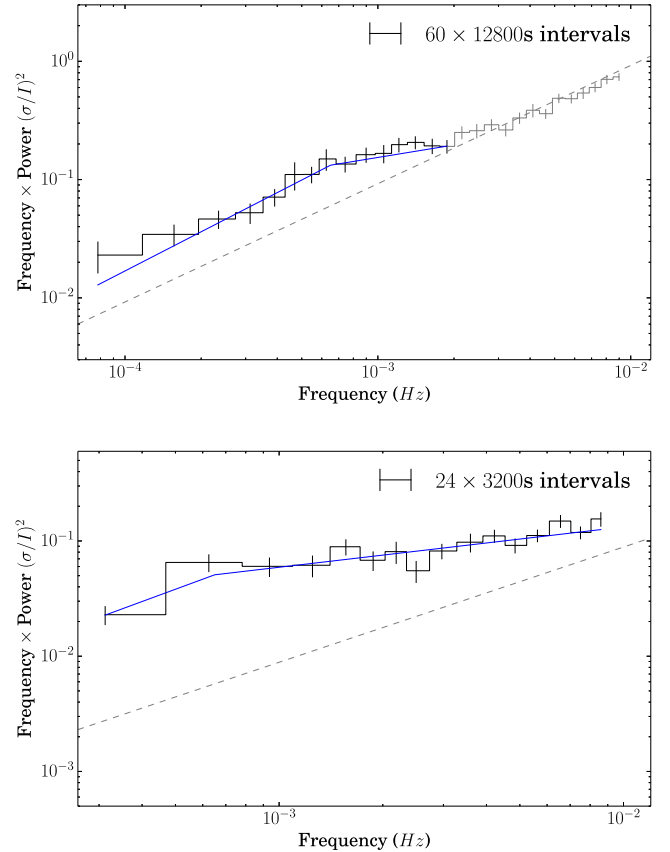

Figure 8. The power spectra for *Chandra* (top) and *XMM–Newton* (bottom) observations, along with the best-fitting broken power-law model in blue (for which $\nu_b = 6.5 \times 10^{-4}$ Hz, $\alpha_1 = -0.1$ and $\alpha_2 = 0.65$), normalized so that power is in units of the squared fractional rms per frequency interval. The white noise level is marked by the dashed grey line, and the bins discounted from analysis due to being dominated by white noise are also coloured grey. The data is geometrically rebinned with a co-efficient of 1.1, and error bars represent the standard error on the mean for each frequency bin.

are other possible counterparts that are too faint or unresolved to characterize. A list of objects and their magnitudes as determined by DAOPHOT II is given in Table 6. Given the faint and crowded nature of the field, we do not expect the values we obtain to be more than approximations.

Using the distance modulus for M51, $\mu = 29.45$, we can calculate an absolute magnitude for each object. We plot M_V against the $B - V$ colour in Fig. 12. Most of the objects that we are able to characterize have low absolute magnitudes (that is, high luminosities) and $B - V$ colours consistent with OB supergiants (Roberts, Levan & Goad 2008) – suitable companion stars for a HMXB – for which we would expect values of M_V of between -7 and -4, and $B - V \sim -0.2$ (Wegner 2006; Roberts et al. 2008). This appears to be consistent with previous findings indicating that ULX optical counterparts are often consistent with being OB-type stars (e.g. Gladstone et al. 2013). We might also expect these properties from an X-ray irradiated disc (e.g. Madhusudhan et al. 2008; Tao et al. 2011). The two exceptions are objects 1 and 9, which are significantly brighter and redder than expected for a OB-type star, and too luminous to be red supergiants (for which we would expect $M_V \sim -6$; Heida et al. 2014). Because of this, it is likely that objects 1 and 9 are small, unresolved clusters of multiple stars. This may also be the case for object 2, as it is also unusually bright.
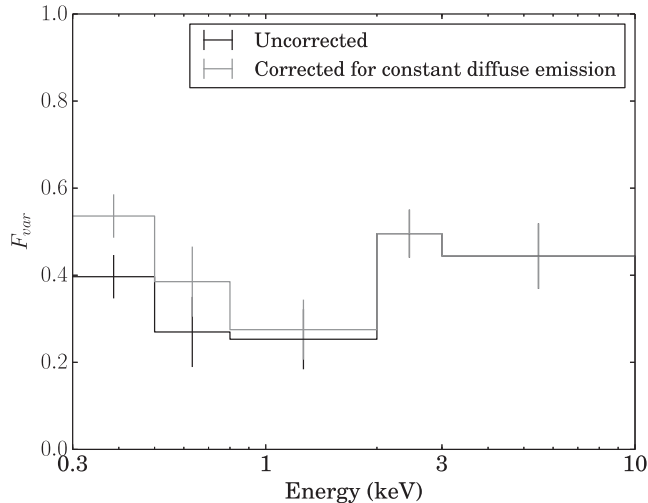
Figure 9. The fractional rms spectrum for ULX-7, both uncorrected (black) and corrected to discount the contribution from non-variable diffuse emission (grey). The energy bands are: 0.3–0.5 keV, 0.5–0.8 keV, 0.8–2.0 keV, 2.0–3.0 keV and 3.0–10.0 keV. The error bars represent the standard error on the mean across all 193 200 s segments.
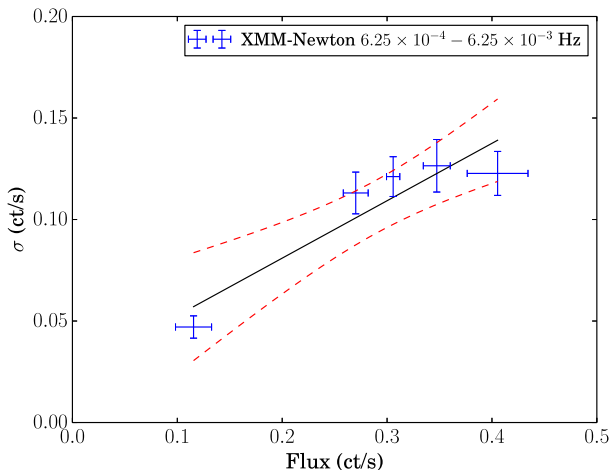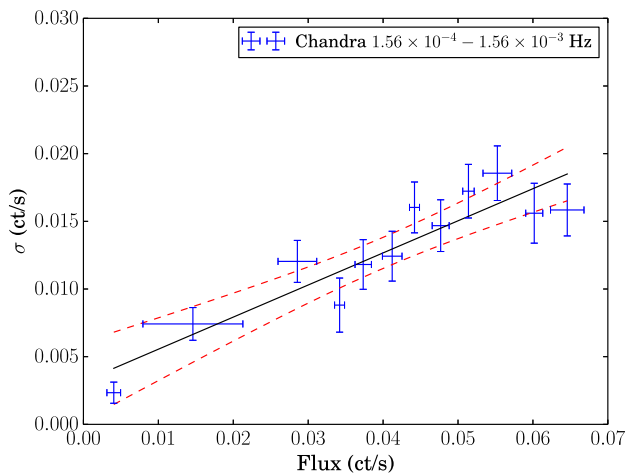

Figure 10. The rms–flux relation for *Chandra* (top) and *XMM–Newton* (bottom) observations, along with a line of best fit (black) and 90 per cent confidence intervals (red dashed). The error bars are the standard deviation of the rms and flux.

Table 5. Periods with $p < 10^{-3}$ found in *XMM–Newton* EPIC-pn data when using the *H*-test to search for pulsations.

ID[a]	Period (s)	p[b] ($\times 10^{-4}$)
X2	0.1833	9.62
X2	0.3003	4.71
X3	0.6211	2.60

[a]The short observation ID as defined in Table 1.
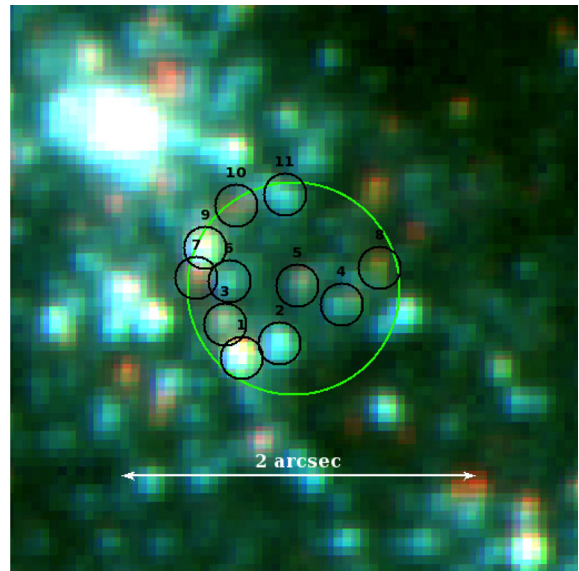[b]The probability of the null hypothesis that there is no periodic signal for this period.

Figure 11. *HST* true-colour image around the position of ULX-7, with the red, green and blue channels corresponding to the *F435W*, *F555W* and *F814W* bands, respectively. A 0.6 arcsec radius circle of 90 per cent confidence is shown around the source position 13:30:01.0 +47:13:44. The numbered objects correspond to those listed in Table 6.

While the colours for the rest of the objects are consistent with OB-type stars, we would also expect background quasars at intermediate redshifts to appear blue, and it would be reasonable to detect them at similar apparent magnitudes to these objects. Therefore, we also calculated an X-ray/optical ratio for the objects, using the highest 2–10 keV flux recorded from ULX-7 and calculating the optical flux using the formula $F_{opt} = 8 \times 10^{-6} \times 10^{-m_V/2.5}$ erg cm^{-2} s^{-1} (e.g. Shtykovskiy & Gilfanov 2005). These ratios are given in Table 6. For any potential counterpart within the error circle that is not characterized by DAOPHOT II, including the faint red objects for which we were unable to determine a *B*- or *V*-band magnitude, the optical flux would be lower therefore the ratio will be higher. The same applies to the brightest characterized counterparts, for although they have the lowest ratios, they are likely to be collections of less luminous objects which will all individually have higher ratios.

4 DISCUSSION

The high luminosity of ULX-7 places it firmly into the category of ULXs, albeit at a luminosity that is not particularly remarkable within that class of sources. What makes ULX-7 remarkable is its unusual spectral and timing properties compared with the majority of ULXs. According to the classification of super-Eddington
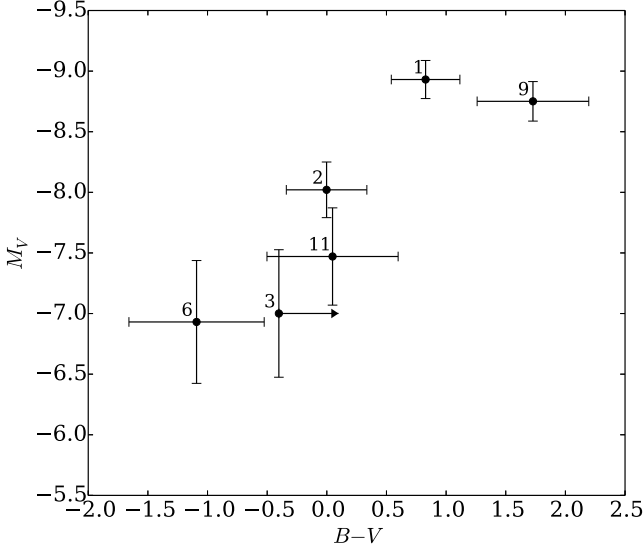
Figure 12. $B - V$ colour against the V-band magnitude for 6 of the 11 potential optical counterparts within 0.6 arcsec of ULX-7, for which we were able to calculate a magnitude for the B and/or V band. Numbers correspond to the ID column of Table 6. Errors are the estimated standard error from DAOPHOT II results.

accretion regimes by Sutton et al. (2013), sources in the hard ultra-luminous regime have very low levels of variability if it is present at all, with high variability only featuring in sources in the soft ultra-luminous regime. Middleton et al. (2015a) suggests that the observed spectrum and variability of sources in ultraluminous accretion states depend on the inclination and accretion rate of the source, with the main driver of these differences being a radiatively driven, massive and inhomogeneous wind, that imprints the variability on the hard component of the spectrum if it rises into the line of sight.

The energy spectrum of ULX-7 could be argued to be consistent with a hard ultraluminous accretion regime, with the characteristic two-component shape expected in the spectrum smeared out by insufficient data quality, except for a hint of a soft excess from *XMM–Newton* observation X3 and a putative high energy turnover in the *NuSTAR* data. However, were the source to truly be in this regime, we would not expect the high levels of variability that we

observe across all observations. This is furthermore unusual given that variability is high at all observed energies, unlike the observed higher variability above 1 keV in the soft ultraluminous regime. Additionally, the observed luminosity of ULX-7 varies by over an order of magnitude, but we see no evidence of the accretion properties changing. Therefore a soft, clumpy wind is unlikely to be the cause of this variability.

It is possible that our understanding of the hard ultraluminous regime of ULXs is as yet incomplete, and that ULX-7 is an unusually variable specimen of this accretion mode. However, as the data quality is insufficient to prefer a more complex spectral model over a power law, we have examined other interpretations for the nature of this object that have power-law-like spectra, in particular considering the scenarios of a background AGN, a super-Eddington neutron star and an IMBH.

4.1 Background AGN

An occasional occurrence in studies of ULXs is the discovery that the object is a background AGN (e.g. Dadina et al. 2013; Sutton et al. 2015), rather than located within the galaxy it appears coincident with. The hard power-law spectrum that we observe is not inconsistent with ULX-7 being an AGN (e.g. Reeves & Turner 2000; Mateos et al. 2010), so we need to look to other source properties to confirm its location.

Examining the possible optical counterparts suggests that this source is likely located within the galaxy. The sources that we are able to characterize are consistent either with OB supergiant type stars, or with clusters of cooler stars. While background quasars at intermediate redshifts could be consistent with the $B - V$ colour and magnitude, we find that for the OB-type stars the X-ray/optical ratios are high, with $F_X/F_{opt} > 10$ in all cases. We would expect the majority of AGNs to have optical/X-ray flux ratios between 0.1 and 10 (e.g. Krautter et al. 1999; Hornschemeier et al. 2001), so it is unlikely that any of these potential optical counterparts are background AGNs. We are only able to characterize the very brightest potential optical counterparts of ULX-7, given the limitations of the data, but since the X-ray/optical relationship would be even higher for the fainter objects we cannot characterize, these are even less likely to be a background AGN.

Table 6. The positions, magnitudes and colours of optical counterparts found within a 0.6 arcsec error circle of 13:30:01.0 +47:13:44, characterized using DAOPHOT II.

ID[a]	RA (J200)	Dec. (J200)	m_B^b	m_V^b	m_I^b	M_V^c	$B - V^c$	$V - I^c$	F_X/F_{opt}^d
1	13 30 01.05	47 13 43.62	22.1 ± 0.2	21.43 ± 0.09	21.04 ± 0.07	-8.9 ± 0.2	0.8 ± 0.3	0.5 ± 0.2	11.7 ± 0.4
2	13 30 01.03	47 13 43.70	22.2 ± 0.2	22.3 ± 0.2	22.8 ± 0.3	-8.0 ± 0.2	0.0 ± 0.3	-0.4 ± 0.4	27.0 ± 0.9
3	13 30 01.06	47 13 43.80	>22.8	23.4 ± 0.5	22.6 ± 0.3	-7.0 ± 0.5	>-0.4	0.8 ± 0.6	69 ± 2
4	13 30 00.99	47 13 43.91	>22.8	>23.5	23.3 ± 0.4	>-6.9	–	>0.3	>76
5	13 30 01.02	47 13 44.03	>22.8	>23.5	23.0 ± 0.3	>-6.9	–	>0.6	>76
6	13 30 01.06	47 13 44.04	22.2 ± 0.2	23.4 ± 0.5	>23.9	-6.9 ± 0.5	-1.1 ± 0.5	<-0.4	73 ± 3
7	13 30 01.07	47 13 44.07	>22.8	>23.5	22.2 ± 0.2	>-6.9	–	>1.3	>76
8	13 30 00.97	47 13 44.12	>22.8	>23.5	23.0 ± 0.4	>-6.9	–	>0.5	>76
9	13 30 01.07	47 13 44.23	23.2 ± 0.4	21.6 ± 0.1	21.5 ± 0.1	-8.8 ± 0.2	1.7 ± 0.5	0.3 ± 0.3	13.8 ± 0.5
10	13 30 01.05	47 13 44.47	>22.8	>23.5	22.7 ± 0.3	>-6.9	–	>0.8	>76
11	13 30 01.03	47 13 44.52	22.8 ± 0.3	22.9 ± 0.4	>23.9	-7.5 ± 0.4	0.0 ± 0.5	<-0.9	45 ± 2

[a]ID for the purposes of reference within this paper only.
[b]Observed magnitude and estimated standard error from DAOPHOT II results, or lower limits where the source was able to be characterized with DAOPHOT II.
[c]Absolute magnitude and colours, corrected for foreground extinction using $E(B - V) = 0.0301 \pm 0.0007$, found using the NASA/IPAC Infrared Science Archive online calculator for Galactic dust and reddening (http://irsa.ipac.caltech.edu/applications/DUST). Values used are from Schlafly & Finkbeiner (2011).
[d]X-ray/optical flux ratio based on the highest detected 2–10 keV flux from ULX-7.

The X-ray/optical relation alone comes with the caveat that we only have one epoch of *HST* data and assume the same optical flux for the highest X-ray flux observation. If the optical emission also varies over time, this conclusion does not necessarily hold. It is also possible that a very highly obscured QSO would have an extreme X-ray/optical flux ratio. However, the proposal that ULX-7 is not a background AGN is also supported by the X-ray timing properties of the source, since there is a high amount of variability on time-scales of ∼100 s. This is shorter than expected for an AGN, for which noise tends to extend only down to time-scales of tens of minutes to hours (e.g. González-Martín & Vaughan 2012). Additionally, the low-frequency break feature we see is also not often seen in AGNs – one exception being Ark 564, which has a break at 7.5×10^{-7} Hz in the 2–8.8 keV band (McHardy et al. 2007), a much lower frequency than the one we see for ULX-7.

4.2 Neutron star

Given the recent discovery that M82 X-2 is in fact a highly super-Eddington pulsar (Bachetti et al. 2014), another possible interpretation for ULX-7's unusual behaviour may be that it is a neutron star rather than a BH. To this end, we searched for coherent pulsations within the *XMM–Newton* data, but found no strong evidence for any between 6.85 and 0.1 Hz with significance comparable to other studies (that is, with $H > 23$). With that said, the absence of pulsations in an *H*-test do not necessarily mean that there is no stellar surface – using a similar method, Doroshenko, Santangelo & Ducci (2015) were unable to detect pulsations from M82 X-2 in the *XMM–Newton* data for the source. It could instead mean that either the pulsation amplitude was too low to be detected, or the spin-down rate and/or orbital modulation of the signal is significant enough to require an accelerated epoch folding search to detect pulsations.

The neutron star equivalent to super-Eddington accreting BHs are Z-sources, the most luminous neutron stars, accreting close to or above their Eddington limit (Hasinger & van der Klis 1989). They can also exhibit high amounts of variability, although at very low frequencies their power spectra exhibit a steep power-law shape with $\alpha \sim 1$–2, inconsistent with the power spectrum of ULX-7, which exhibits a low break and a flatter slope. A comparison with the very luminous extragalactic Z-source LMC X-2, located in the Large Magellanic Cloud, further reveals that its energy spectrum is harder than that of ULX-7 as well (Barnard et al. 2015), so the properties of ULX-7 appear to be inconsistent with what we would expect from Z-sources.

However, the recently reported spectral properties of M82 X-2 (Brightman et al. 2015) indicate that it is possible for a super-Eddington neutron star ULX to show similar properties to ULX-7. As well as long-term flux variations over two orders of magnitude, examination of the pulsed spectrum in *NuSTAR* shows that the spectrum of M82 X-2 has a high energy turnover at 14^{+5}_{-3} keV. Further observations using *NuSTAR* would help to confirm whether ULX-7 exhibits a similar spectral shape at high energies.

4.3 Intermediate mass BH

Another possible interpretation is that ULX-7 is instead a BH accreting in a hard state analogous to lower luminosity BHBs. This would imply an unusually high BH mass due to its high luminosity, despite a low assumed accretion rate, and would manifest a hard power-law shaped spectrum with high variability across all energy bands (e.g. Grinberg et al. 2014) like we see in ULX-7. The irradiated disc of an IMBH would also be consistent with most of the possible optical counterparts we detect (Madhusudhan et al. 2008).

This interpretation is supported by the presence of a break in the power spectrum from a spectral index of $\alpha \sim 0$ to $\alpha \sim 1$, a feature that we would expect from the low-frequency break in the power spectrum of a source in the hard state, which can be modelled by two Lorentzians or, more simply, a doubly broken power law (e.g. Done & Gierliński 2005), whose high-frequency break scales with the BH mass. While we see no evidence of a high-frequency break, we can take the lower limit of such a break to be the white noise level of the *XMM–Newton* power spectrum, at $\nu_b = 9 \times 10^{-3}$ Hz. We can use the relationship between high-frequency break and BH mass found to apply to BHs of all size scales by McHardy et al. (2006), with the offset for BHs in the hard state from Körding et al. (2007), to calculate an upper limit on the BH mass using the following equation: $\log \nu_b = 0.98 \log \dot{M} - 2.1 \log M_{BH} - 15.38$. We calculate $\dot{M}$ from $L_{bol}/\eta c^2$, assuming an accretion efficiency of $\eta = 0.1$ for the highest flux observation, and obtain L_{bol} by applying a bolometric correction of 5 to the 2–10 keV luminosity of that observation (Körding, Fender & Migliari 2006). In this way, we find an upper limit of $M_{BH} < 1.6 \times 10^3$ M$_\odot$, which means that ULX-7 is consistent with being an IMBH.

We would expect an IMBH accreting in the hard state to also exhibit radio emission from a jet. Since there is no radio detection of ULX-7, we can use the calculated flux density upper limit of 87 μJy beam^{-1} to establish an upper limit on the BH mass independent of that calculated from the timing analysis, using the Fundamental Plane in BH mass, radio and X-ray luminosity which has been found to apply to BHBs and AGNs as well as intermediate sources (e.g. Mezcua et al. 2015). We use the Fundamental Plane equation described in Gültekin et al. (2009), which has been calibrated for low mass AGNs in the range 10^5–10^7 M$_\odot$ (Gültekin et al. 2014), and assume a flat radio spectral index of $\alpha = 0.15$ to find $L_{5\,GHz}$. We calculate a mass upper limit of $M_{BH} < 3.5 \times 10^4$ M$_\odot$, which also allows for an IMBH interpretation.

It is also possible to place a lower limit on the BH mass of an IMBH by taking the maximum observed flux of 8.6×10^{-13} erg cm^{-2} s^{-1} and assuming a maximum accretion rate for the low/hard state, given that ULX-7 is a persistent source. The maximum luminosity of a low/hard state tends to be ∼2 per cent of Eddington,[5] with the highest Eddington ratios observed being ∼5 per cent (Maccarone 2003). Therefore, we use an Eddington ratio of 5 per cent to place a lower limit on the BH mass of $M_{BH} > 1.0 \times 10^3$ M$_\odot$, which is consistent with our previously calculated upper limits and places the source firmly within the IMBH regime.

We can compare our results for ULX-7 with HLX-1, currently the best candidate for an IMBH due to its extreme luminosity and evidence of state transitions. When first discovered, it had a spectrum consistent with an absorbed power law (Farrell et al. 2009), albeit a softer one than we see in ULX-7. Further studies have revealed it to have a very high dynamic range, as we see for ULX-7, although its spectrum changes shape and it appears to demonstrate state transitions (Godet et al. 2009) whereas ULX-7 appears to remain in a single state. In its third *XMM–Newton* observation, HLX-1

---

[5] It is possible for transient BHs in the hard state to reach up to 100 per cent of Eddington before a transition to the soft thermal state (Dunn et al. 2010), however given that we see no evidence of state transitions for ULX-7, we calculate the lower limit using a more typical value for persistent hard states.

appeared to enter a hard state, with a lower luminosity and a spectral index of $\Gamma = 1.6 \pm 0.4$ when compensating for the host galaxy's contribution to the soft emission and fitted alongside an accretion disc (Servillat et al. 2011). No significant intrinsic variability was detected, although since the power was not well constrained, a high fractional variability was not ruled out. Additionally, there have also been radio detections of HLX-1 while in this state (Cseh et al. 2015), making it analogous to the hard state seen in stellar-mass BHBs.

From this, we can conclude that it is reasonable to suggest that ULX-7 could also be an IMBH in a hard state, its large mass being the cause of its high luminosities, although unlike HLX-1, it does not appear to undergo state transitions as it changes luminosity.

The association of ULX-7 with a young stellar population implies that it is a short-lived source if it was formed there (Roberts 2007), and in this respect it bears similarity to the wider ULX population which is found predominantly in star-forming regions. This would be a point in favour of a more standard stellar remnant ULX interpretation. However, there are possible formation scenarios for an IMBH in a young stellar environment. For example, an IMBH could have formed through runaway mergers within a dense stellar cluster and subsequently been ejected, or the cluster dissipated into the disc of the galaxy, leaving the IMBH accreting within a dense molecular cloud (e.g. Miller & Hamilton 2002) or retaining a young stellar population around itself (e.g. Farrell et al. 2012). This is an unlikely formation scenario for the ULX population as a whole (King 2004), but still a possibility for an individual object, as a very rare occurrence.

Another possibility is a minor merger of a dwarf galaxy with the main galaxy, a mechanism that has been suggested for HLX-1 (Farrell et al. 2012; Mapelli, Zampieri & Mayer 2012) and NGC 2276-3c (Mezcua et al. 2015). A recent minor merger could be identified by evidence of disruption in the spiral arm around the source and increased levels of star formation, however these are seen in the northern spiral of M51 anyway due to M51a's interaction with M51b. Therefore any evidence for a minor merger that could have formed ULX-7 would likely be eclipsed by the disruption of the current interaction.

5 CONCLUSIONS

We have undertaken a case study of M51 ULX-7, a source with moderate luminosity and very high variability for a ULX, and a consistently hard spectrum. This is in contrast to expected ULX variability behaviour, in which we might expect to see high variability in sources with soft spectra. We find that the source is generally well-fitted by a power law with a spectral photon index that remains steady at $\Gamma \sim 1.5$ while the source luminosity varies by over an order of magnitude over the course of 12 yr. ULX-7 also demonstrates very high fractional variability between 0.3 and 10.0 keV, with a broken power-law shape to its power spectrum analogous to the low-frequency break in the power spectrum of an X-ray binary accreting in the hard state. We find solid evidence for a positive linear rms–flux relation, making ULX-7 the third ULX for which this feature is confirmed. We find no evidence of coherent pulsations, however.

Taken together, these properties are unusual for a ULX, and are suggestive of an alternative explanation to the broadened disc or ultraluminous regimes that describe the majority of ULXs for which we have reasonable data (Gladstone et al. 2009; Sutton et al. 2013). By examining the possible optical counterparts in *HST* data, we consider it unlikely that this source is a background AGN. The lack of pulsations and dissimilarity to Z-source properties imply that it is not a neutron star either, although it may possibly bear similarities to the properties of the neutron star ULX M82 X-2.

Our results are consistent with ULX-7 being an IMBH accreting in the hard state. Using the absence of a high-frequency break and a radio detection, we can calculate upper limits on the BH mass of $M_{BH} < 1.55 \times 10^3$ M$_\odot$ and $M_{BH} < 3.5 \times 10^4$ M$_\odot$, respectively, and by taking the maximum accretion rate to be 5 per cent of the Eddington limit, we can calculate a lower mass limit of $M_{BH} > 1.0 \times 10^3$ M$_\odot$. All of these limits show the source to be consistent with an IMBH interpretation if we assume it is accreting in the hard state. There remains weak evidence of a possible high energy turnover in the spectrum when considering the *NuSTAR* data on this source, which would imply that this source may instead be exhibiting some permutation of the ultraluminous state after all, but simultaneous deep observations with *XMM–Newton* and *NuSTAR* will be required to confirm or rule out the existence of these features.

REFERENCES

Abolmasov P., Fabrika S., Sholukhova O., Afanasiev V., 2007, Astrophys. Bull., 62, 36
Arnaud K. A., 1996, in Jacoby G. H., Barnes J., eds, ASP Conf. Ser. Vol. 101, Astronomical Data Analysis Software and Systems V. Astron. Soc. Pac., San Francisco, p. 17
Bachetti M. et al., 2013, ApJ, 778, 163
Bachetti M. et al., 2014, Nature, 514, 202
Barnard R., Primini F., Garcia M. R., Kolb U. C., Murray S. S., 2015, ApJ, 802, 85
Brightman M. et al., 2015, preprint (arXiv:e-prints)
Buccheri R. et al., 1983, A&A, 128, 245
Colbert E. J. M., Mushotzky R. F., 1999, ApJ, 519, 89
Cseh D. et al., 2015, MNRAS, 446, 3268
Dadina M., Masetti N., Cappi M., Malaguti G., Miniutti G., Ponti G., Gandhi P., De Marco B., 2013, A&A, 559, A86
de Jager O. C., Raubenheimer B. C., Swanepoel J. W. H., 1989, A&A, 221, 180

de Vaucouleurs G., de Vaucouleurs A., Corwin H. G., Jr, Buta R. J., Paturel G., Fouqué P., 1991, Third Reference Catalogue of Bright Galaxies. Volume I: Explanations and references. Volume II: Data for galaxies between 0^h and 12^h. Volume III: Data for galaxies between 12^h and 24^h.

Dewangan G. C., Griffiths R. E., Choudhury M., Miyaji T., Schurch N. J., 2005, ApJ, 635, 198

Done C., Gierliński M., 2005, MNRAS, 364, 208

Doroshenko V., Santangelo A., Ducci L., 2015, A&A, 579, A22

Dunn R. J. H., Fender R. P., Körding E. G., Belloni T., Cabanac C., 2010, MNRAS, 403, 61

Farrell S. A., Webb N. A., Barret D., Godet O., Rodrigues J. M., 2009, Nature, 460, 73

Farrell S. A. et al., 2012, ApJ, 747, L13

Feng H., Kaaret P., 2005, ApJ, 633, 1052

Feng H., Soria R., 2011, New Astron. Rev., 55, 166

Gao Y., Wang Q. D., Appleton P. N., Lucas R. A., 2003, ApJ, 596, L171

Gladstone J. C., Roberts T. P., Done C., 2009, MNRAS, 397, 1836

Gladstone J. C., Copperwheat C., Heinke C. O., Roberts T. P., Cartwright T. F., Levan A. J., Goad M. R., 2013, APJS, 206, 14

Godet O., Barret D., Webb N. A., Farrell S. A., Gehrels N., 2009, ApJ, 705, L109

González-Martín O., Vaughan S., 2012, A&A, 544, A80

Grinberg V. et al., 2014, A&A, 565, A1

Gültekin K., Cackett E. M., Miller J. M., Di Matteo T., Markoff S., Richstone D. O., 2009, ApJ, 706, 404

Gültekin K., Cackett E. M., King A. L., Miller J. M., Pinkney J., 2014, ApJ, 788, L22

Hasinger G., van der Klis M., 1989, A&A, 225, 79

Heida M. et al., 2014, MNRAS, 442, 1054

Heil L. M., Vaughan S., Roberts T. P., 2009, MNRAS, 397, 1061

Heil L. M., Vaughan S., Uttley P., 2012, MNRAS, 422, 2620

Hernández-García L., Vaughan S., Roberts T. P., Middleton M., 2015, MNRAS, 453, 2877

Hornschemeier A. E. et al., 2001, ApJ, 554, 742

Kajava J. J. E., Poutanen J., 2009, MNRAS, 398, 1450

Kalberla P. M. W., Burton W. B., Hartmann D., Arnal E. M., Bajaja E., Morras R., Pöppel W. G. L., 2005, A&A, 440, 775

Kilgard R. E. et al., 2005, APJS, 159, 214

King A. R., 2004, MNRAS, 347, L18

King A. R., Davies M. B., Ward M. J., Fabbiano G., Elvis M., 2001, ApJ, 552, L109

Körding E. G., Fender R. P., Migliari S., 2006, MNRAS, 369, 1451

Körding E. G., Migliari S., Fender R., Belloni T., Knigge C., McHardy I., 2007, MNRAS, 380, 301

Krautter J. et al., 1999, A&A, 350, 743

Liu J.-F., Bregman J. N., Irwin J., Seitzer P., 2002, ApJ, 581, L93

Maccarone T. J., 2003, A&A, 409, 697

McHardy I. M., Koerding E., Knigge C., Uttley P., Fender R. P., 2006, Nature, 444, 730

McHardy I. M., Arévalo P., Uttley P., Papadakis I. E., Summons D. P., Brinkmann W., Page M. J., 2007, MNRAS, 382, 985

Madau P., Rees M. J., 2001, ApJ, 551, L27

Maddox L. A., Cowan J. J., Kilgard R. E., Schinnerer E., Stockdale C. J., 2007, AJ, 133, 2559

Madhusudhan N., Rappaport S., Podsiadlowski P., Nelson L., 2008, ApJ, 688, 1235

Mapelli M., Zampieri L., Mayer L., 2012, MNRAS, 423, 1309

Mateos S. et al., 2010, A&A, 510, A35

Mezcua M., Roberts T. P., Sutton A. D., Lobanov A. P., 2013, MNRAS, 436, 3128

Mezcua M., Roberts T. P., Lobanov A. P., Sutton A. D., 2015, MNRAS, 448, 1893

Middleton M. J., Roberts T. P., Done C., Jackson F. E., 2011, MNRAS, 411, 644

Middleton M. J. et al., 2013, Nature, 493, 187

Middleton M. J., Heil L., Pintore F., Walton D. J., Roberts T. P., 2015a, MNRAS, 447, 3243

Middleton M. J., Walton D. J., Fabian A., Roberts T. P., Heil L., Pinto C., Anderson G., Sutton A., 2015b, MNRAS, 454, 3134

Miller M. C., Hamilton D. P., 2002, MNRAS, 330, 232

Mineo S., Gilfanov M., Sunyaev R., 2012, MNRAS, 419, 2095

Miyawaki R., Makishima K., Yamada S., Gandhi P., Mizuno T., Kubota A., Tsuru T. G., Matsumoto H., 2009, PASJ, 61, 263

Owen R. A., Warwick R. S., 2009, MNRAS, 394, 1741

Özel F., Psaltis D., Narayan R., McClintock J. E., 2010, ApJ, 725, 1918

Poutanen J., Lipunova G., Fabrika S., Butkevich A. G., Abolmasov P., 2007, MNRAS, 377, 1187

Rampadarath H., Morgan J. S., Soria R., Tingay S. J., Reynolds C., Argo M. K., Dumas G., 2015, MNRAS, 452, 32

Reeves J. N., Turner M. J. L., 2000, MNRAS, 316, 234

Roberts T. P., 2007, Ap&SS, 311, 203

Roberts T. P., Levan A. J., Goad M. R., 2008, MNRAS, 387, 73

Rosen S. et al., 2015, in Taylor A. R., Rosolowsky E., eds, ASP Conf. Ser. Vol. 495, Astronomical Data Analysis Software an Systems XXIV. Astron. Soc. Pac., San Francisco, p. 319

Schlafly E. F., Finkbeiner D. P., 2011, ApJ, 737, 103

Servillat M., Farrell S. A., Lin D., Godet O., Barret D., Webb N. A., 2011, ApJ, 743, 6

Shtykovskiy P., Gilfanov M., 2005, MNRAS, 362, 879

Stetson P. B., 1987, PASP, 99, 191

Stobbart A.-M., Roberts T. P., Wilms J., 2006, MNRAS, 368, 397

Sutton A. D., Roberts T. P., Walton D. J., Gladstone J. C., Scott A. E., 2012, MNRAS, 423, 1154

Sutton A. D., Roberts T. P., Middleton M. J., 2013, MNRAS, 435, 1758

Sutton A. D., Roberts T. P., Gladstone J. C., Walton D. J., 2015, MNRAS, 450, 787

Swartz D. A., Ghosh K. K., Tennant A. F., Wu K., 2004, APJS, 154, 519

Swartz D. A., Soria R., Tennant A. F., Yukita M., 2011, ApJ, 741, 49

Tao L., Feng H., Grisé F., Kaaret P., 2011, ApJ, 737, 81

Terashima Y., Wilson A. S., 2004, ApJ, 601, 735

Terashima Y., Inoue H., Wilson A. S., 2006, ApJ, 645, 264

Walton D. J., Roberts T. P., Mateos S., Heard V., 2011, MNRAS, 416, 1844

Walton D. J. et al., 2015, ApJ, 799, 122

Wegner W., 2006, MNRAS, 371, 185

Wilms J., Allen A., McCray R., 2000, ApJ, 542, 914

Yoshida T., Ebisawa K., Matsushita K., Tsujimoto M., Kawaguchi T., 2010, ApJ, 722, 760

This paper has been typeset from a TeX/LaTeX file prepared by the author.